NANO · MICRO
small
www.small-journal.com

Low-Temperature ALD of SbO_x/Sb_2Te_3 Multilayers with Boosted Thermoelectric Performance

Jun Yang, Samik Mukherjee, Sebastian Lehmann, Fabian Krahl, Xiaoyu Wang, Pavel Potapov, Axel Lubk, Tobias Ritschel, Jochen Geck, and Kornelius Nielsch**

Nanoscale superlattice (SL) structures have proven to be effective in enhancing the thermoelectric (TE) properties of thin films. Herein, the main phase of antimony telluride (Sb_2Te_3) thin film with sub-nanometer layers of antimony oxide (SbO_x) is synthesized via atomic layer deposition (ALD) at a low temperature of 80 °C. The SL structure is tailored by varying the cycle numbers of Sb_2Te_3 and SbO_x. A remarkable power factor of 520.8 µW m^{-1} K^{-2} is attained at room temperature when the cycle ratio of SbO_x and Sb_2Te_3 is set at 1:1000 (i.e., SO:ST = 1:1000), corresponding to the highest electrical conductivity of 339.8 S cm^{-1}. The results indicate that at the largest thickness, corresponding to ten ALD cycles, the SbOx layers act as a potential barrier that filters out the low-energy charge carriers from contributing to the overall electrical conductivity. In addition to enhancing the scattering of the mid-to-long-wavelength at the SbO_x/Sb_2Te_3 interface, the presence of the SbO_x sub-layer induces the confinement effect and strain forces in the Sb_2Te_3 thin film, thereby effectively enhancing the Seebeck coefficient and reducing the thermal conductivity. These findings provide a new perspective on the design of SL-structured TE materials and devices.

1. Introduction

The prospect of a direct interconversion between thermal and electrical energies in thermoelectric (TE) materials has garnered significant interest in various areas including the exploration of new materials, fundamental transport studies, novel device architectures, and optimization of device performance.[1] The development of efficient thermoelectric materials holds great promise in addressing longstanding challenges in carbon-free energy harvesting, heat scavenging, and thermoelectric refrigeration applications.[2] A good TE material should possess the following essential qualities: high electrical conductivity (σ) to minimize the internal Joule loss, high Seebeck coefficient (S) to generate high output voltages, and low thermal conductivity (κ) to maintain the temperature gradient across its ends. The efficacy of a material as a TE energy converter is evaluated using a dimensionless figure-of-merit, $ZT = \sigma S^2 T/(\kappa_E+\kappa_L)$, where T is the average temperature between the hot and the cold ends, κ_E and κ_L are the contributions of the charge carriers and lattice, respectively, to the total value of κ. Optimizing the TE power factor (PF) (σS^2) in any material requires precise tunability of the most essential transport parameter. A high power factor in thermoelectric materials signifies their ability to efficiently convert a temperature difference into electrical power.[3] It leads to increased power output, improved energy conversion efficiency, minimized energy losses, and optimal power transfer, making high power factor thermoelectric materials highly desirable for various applications. However, these

---

J. Yang, S. Mukherjee, S. Lehmann, F. Krahl, K. Nielsch
Institute for Metallic Materials
Leibniz Institute for Solid State and Materials Research
01069 Dresden, Germany
E-mail: j.yang@ifw-dresden.de; k.nielsch@ifw-dresden.de

J. Yang, K. Nielsch
Institute of Materials Science
Technische Universität Dresden
01062 Dresden, Germany

S. Mukherjee
Jio Institute
Navi Mumbai, Maharashtra 410206, India

X. Wang
Institute for Integrative Nanosciences
Leibniz Institute for Solid State and Materials Research
01069 Dresden, Germany

X. Wang
School of Physics and Optoelectronic Engineering
Hainan University
Haikou 570228, China

P. Potapov, A. Lubk
Institute for Solid State Research
Leibniz Institute for Solid State and Materials Research
01069 Dresden, Germany

T. Ritschel, J. Geck
Institute of Solid State and Materials Physics
Technische Universität Dresden
01069 Dresden, Germany

The ORCID identification number(s) for the author(s) of this article can be found under https://doi.org/10.1002/smll.202306350

© 2023 The Authors. Small published by Wiley-VCH GmbH. This is an open access article under the terms of the Creative Commons Attribution License, which permits use, distribution and reproduction in any medium, provided the original work is properly cited.

DOI: 10.1002/smll.202306350

parameters are intricately interconnected in any solid-state materials, making it challenging to independently fine-tune them. As a result, despite extensive exploration of various material classes, such as tellurides, antimonides, oxide-based materials, Heuslers and half-Heuslers, Zintl phases, organic polymers, and silicon-germanium alloys for TE applications, the output power of TE energy conversion has remained relatively low for an extended period, limiting its widespread adoption beyond a few specialized domains.[4]

Since the early predictions by Hicks and Dresselhaus,[5,6] exploring the quantum effects and scattering effects in nanostructured materials has emerged as a powerful paradigm to circumvent some of the inherent issues related to the transport processes in TE materials.[7] Superlattices (SLs) belong to a class of nanomaterials that comprises periodic alternating layers of two different materials. The artificial periodicity brought about by the layered structure can lead to mini-band formation in the electronic band structure due to the folding of the Brillouin zone.[8] In addition, interfaces can also play a crucial role in influencing the transport properties in SLs. Theoretical studies indicate that phonons can scatter at the interfaces either specularly or diffusively, or a combination of both.[9,10] Interfacial scattering in ultrathin SLs can, in principle, cause phonon interference phenomena and Anderson localization-like behavior of low-frequency phonons and reduce thermal conductivity.[9]

Sb_2Te_3 is a 2D topological insulator (TI), that exhibits gapless Dirac surface states as a result of the nontrivial topology of the electronic wavefunction in the bulk.[11] Like a lot of other TIs, Sb_2Te_3 also shows promising TE properties owing to the presence of heavy elements and narrow band gaps. Additionally, the high surface-area-to-volume ratio of low-dimensional nanostructured thin films offers the potential to suppress the bulk transport effect and enhance the efficiency of thermoelectric devices.[5] Winkler et al. synthesized Sb_2Te_3 (5 nm)/Bi_2Te_3 (1 nm) superlattice structure and achieved an ultralow lattice thermal conductivity of 0.23 W m^{-1} K^{-1}.[12] Lee et al. investigated a p-type $Bi_{0.5}Sb_{1.5}Te_3/Bi_2Te_3$ superlattice film and achieved a satisfactory power factor value of 4.4 μW m^{-1} K^{-2} due to the low interfacial resistance of the superlattice structure.[13] Hu et al. fabricated Sb_2Te_3/metal (Cu, Ag, Au, Pt) multilayer thin films and observed a significant reduction in thermal conductivity without compromising electron transfer properties by optimizing the material system.[14] The atomic layer deposition (ALD) technique offers the highest conformality, as well as atomic-level precision in the film thickness over a wide deposition temperature range, owing to sequential and self-limiting surface reactions.[15] Earlier reports have demonstrated that the doping insulator layer can enhance the TE properties of semiconductor materials by filtering carrier transportation.[16,17] SbO_x possesses excellent dielectric properties and has great potential for the application of microelectronic devices.[18,19] Moreover, SbO_x exhibits an amorphous structure, which eliminates lattice mismatch with the crystallized Sb_2Te_3.

Here, SbO_x/Sb_2Te_3 (SO/ST) multilayer thin films, which we also call Ferecrystals, with different periodicities were deposited by a thermal ALD reactor at a low temperature of 80 °C. The crystal structure and thermal transport properties of the superlattice structure were systematically studied. Compared to the initial Sb_2Te_3 (291.9 S cm^{-1}), the sample 1000 cycles of Sb_2Te_3 with one cycle of SbO_x (SO:ST = 1:1000) showed a higher electrical conductivity of 339.8 S cm^{-1}. When the continuous SbO_x film was integrated into the Sb_2Te_3 system, a potential barrier was formed, filtering low-energy carriers. The thermal conductivity (especially lattice thermal conductivity) of the superlattice structure of SbO_x/Sb_2Te_3 was suppressed due to the enhanced scattering of the mid-to-long wavelength phonons and the introduction of lattice strain. This study provides a fresh perspective on enhancing the thermoelectric performance of thin films using ALD.

2. Results and Discussion

The growth behaviors of single-phase Sb_2Te_3 and SbO_x were investigated prior to the synthesis of the multilayered structure. For the fabrication of Sb_2Te_3 films, the precursors $SbCl_3$ and $(Et_3Si)_2Te$ were utilized, whereas $Sb(OEt)_3$ and $SbCl_3$ were employed for the synthesis of SbO_x films. In order to obtain a good interface between Sb_2Te_3 and SbO_x, the thin films were deposited at the same reactor temperature of 80 °C without any vacuum break (see more details in the Experimental Section). Sb_2Te_3 thin film is the main phase of the SL structure with different sub-cycle numbers of the SbO_x layer. The electrical transport properties of SO/ST heterostructure were measured with the different sub-cycle numbers of SbO_x, with temperatures ranging from 293 to 473 K, as shown in **Figure 1**. The carrier concentration and electrical conductivity using Hall measurement are shown in Figure 1a,b. At the measurement temperature of 293 K, the carrier concentration (n) of Sb_2Te_3 is 1.16×10^{19} cm^{-3}. The SO/ST = 1:1000 sample (1000 cycles of Sb_2Te_3 is with one cycle of SbO_x and the supercycle number is 5) exhibited a higher n (1.37×10^{19} cm^{-3}) than that of Sb_2Te_3 films. However, when the ALD cycles of the Sb_2Te_3 layers in the SL were reduced from 1000 to 600, the n significantly decreased to 9.20×10^{18} cm^{-3}. The minimum carrier concentration was 6.00×10^{18} cm^{-3} for the sample of SO:ST = 1:150 at 293 K. A similar trend was also observed for electrical conductivity (σ). For example, the highest conductivity of 339.8 S cm^{-1} was obtained for the sample of SO:ST = 1:1000, which is higher than that of the Sb_2Te_3 film (291.9 S cm^{-1}). In contrast, the SO:ST = 1:150 sample shows the lowest conductivity of 243.2 S cm^{-1} at 293 K. The mobility increases with SbO_x doping and reaches 255 cm^2 Vs^{-1} at room temperature when SO:ST = 1:150 due to the higher crystalline ordering (Figure S2, Supporting Information).

The temperature-dependent Seebeck coefficients (S) of SO/ST SLs are shown in Figure 1c, suggesting a clear p-type behavior with holes as main charge carriers. The relation between S and n can be described by Equations (1) and (2)[20]

$$S = \frac{k_B}{e}\left(s + \frac{5}{2} + \ln \frac{2 \times \left(2\pi m^* k_B\right)^{3/2}}{nh^3}\right) \tag{1}$$

$$S = \frac{k_B}{e}\ (s - \ln n) + C \tag{2}$$

where k_B is the Boltzmann constant, h is the Planck constant, m^* is the effective mass, s is the scattering parameter, and C is a constant. The Seebeck coefficient is inversely proportional to

© 2023 The Authors. Small published by Wiley-VCH GmbH

16136829, 2024, 10, Downloaded from https://onlinelibrary.wiley.com/doi/10.1002/smll.202306350, Wiley Online Library on [13/04/2024]. See the Terms and Conditions (https://onlinelibrary.wiley.com/terms-and-conditions) on Wiley Online Library for rules of use; OA articles are governed by the applicable Creative Commons License

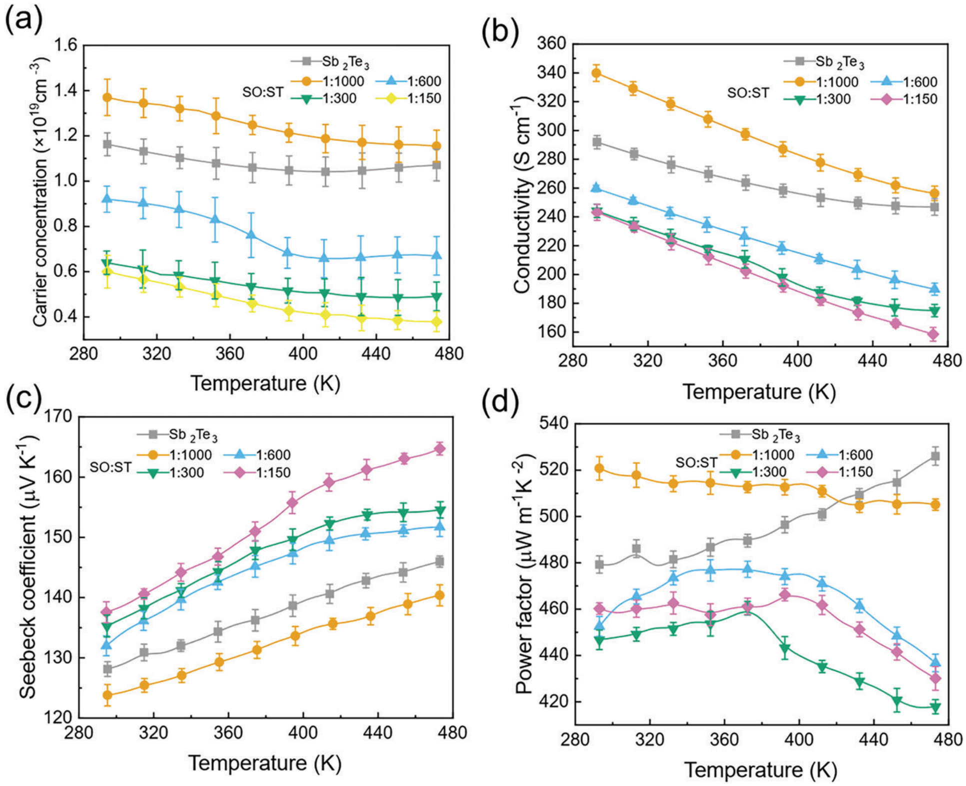

Figure 1. Transport properties of SbO_x/Sb_2Te_3 multilayers in the temperature range 293 to 473 K: a) carrier concentration, b) conductivity, c) Seebeck coefficient, and d) power factor.

free charge carrier concentration, meaning that an increased carrier concentration leads to a reduction in S. As observed, a high Seebeck of 164.7 μV K^{-1} was achieved at the temperature of 473 K for the SO:ST = 1:150 sample due to the lower carrier concentration compared with other samples. The as-achieved properties exhibited high repeatability (Figure S3, Supporting Information). The PF was calculated based on the electrical conductivity and Seebeck coefficient results (Figure 1d). The SO:ST = 1:1000 sample attained a high power factor value of 520.8 μW m^{-1} K^{-2} at 293 K. At low temperatures, the power factor of SO/ST = 1:1000 surpasses that of the Sb_2Te_3 sample. Conversely, at high temperatures, the situation is reversed, with the power factor of SO/ST = 1:1000 being lower than that of Sb_2Te_3. This discrepancy arises due to the distinct temperature-dependent conductivity trends exhibited by both thin films. In the lower temperature range (300–420 K), the conductivity of SO/ST = 1:1000 significantly surpasses that of Sb_2Te_3, which primarily accounts for the higher power factor observed in SO/ST = 1:1000 within this temperature range. However, as the temperature increases (420–473 K), the conductivity of SO/ST = 1:1000 experiences a rapid decline, whereas the conductivity decrease in Sb_2Te_3 is comparatively gradual. Notably, within the high-temperature range, Sb_2Te_3 thin films undergo an electronic topological transition, resulting in a pronounced redistribution of the electronic density of states near the Fermi level, thereby enhancing electrical transport parameters.[21] In contrast, SO/ST = 1:1000 samples exhibit a lesser degree of electronic topological transition due to the presence of the SbO_x buffer layer.[22] Since $PF = \sigma S^2$, the conductivity of Sb_2Te_3 exhibits a gradual reduction in the high-temperature region, leading to a higher power factor. Conversely, doped Sb_2Te_3 experiences a rapid decline in conductivity, resulting in a lower power factor.

To further analyze the structural characteristics of the samples, grazing incidence X-ray diffraction (GID) measurements were performed using a custom-made laboratory setup with a Mo *Kα* source. The corresponding data are presented in **Figure 2**. The as-deposited Sb_2Te_3 attains a flaked structure which is also evident from scanning electron microscopy (Figure 2f). In the GID data for the SO:ST = 10:1000 sample, these randomly oriented flakes lead to Laue cones with very weak texture, as can be seen in Figure 2a,c. However, with increasing SO:ST cycle ratio, that is, with decreasing Sb_2Te_3 layer thickness, sharp peaks emerge from the Laue rings, indicative of a high textured film structure (Figure 2b,c). This indicates that with increasing SbO_x film thickness the flakes tend to align with respect to each other according to a preferred orientation. On the other hand, the peak width in the θ–2θ direction changes only slightly from 0.65° to 0.5° when the cycle ratio SO:ST increases from 10:1000 to 10:600 as can be seen in Figure 2e. For even larger SO:ST the peak width remains almost constant. Therefore, the crystallinity of the flakes itself is not significantly affected by the SO:ST cycle ratio.

The morphology of the Sb_2Te_3 flake can also affect the thermoelectric properties. The contact resistance arises at the junction between flakes due to the nanogap and weak contact.[23] The ultrathin SbO_x can act as a bridge and provide a pathway for carrier transportation to enhance the electrical conductivity, as

© 2023 The Authors. Small published by Wiley-VCH GmbH

16136829, 2024, 10, Downloaded from https://onlinelibrary.wiley.com/doi/10.1002/smll.202306350, Wiley Online Library on [13/04/2024]. See the Terms and Conditions (https://onlinelibrary.wiley.com/terms-and-conditions) on Wiley Online Library for rules of use; OA articles are governed by the applicable Creative Commons License

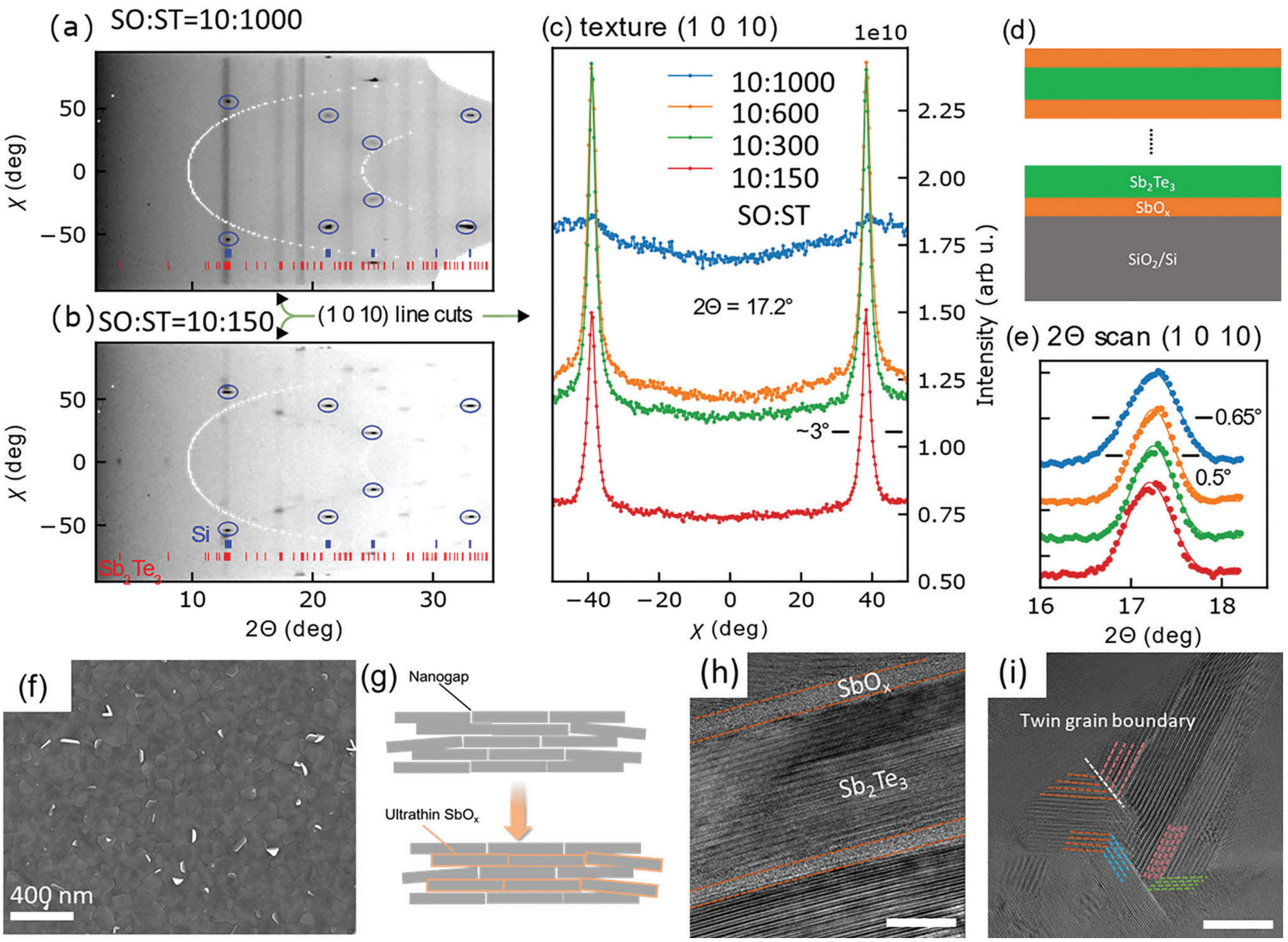

Figure 2. Gracing incident X-ray diffraction of SbO_x/Sb_2Te_3 heterostructures with different cycle ratios SO:ST. a,b) Regrouped scattered X-ray intensity as a function of scattering angle 2θ and polar angle X, that is, angle along the Laue cone. c) Line scan at a constant 2θ angle of 17.2° for different cycle ratios SO:ST. d) Sketch of the SbO_x/Sb_2Te_3 multilayer structure. e): θ–2θ scan through the (1 0 10) peak for different cycle ratios (corrected for background, normalized, and offset for better visualization). f) SEM image of Sb_2Te_3 thin film. g) The schematic illustration of Sb_2Te_3 flakes after SbO_x coating. h) The typical cross-section and i) twin grain boundary TEM images of SbO_x/Sb_2Te_3 heterostructure (scale bar: 10 nm).

schematized in Figure 2g. Meanwhile, an Sb-rich environment was formed during the ALD process. Since the SbO_x precursors, $SbCl_3$ and $Sb(OEt)_3$, both contain Sb. We speculate that the preliminary cycle of SbO_x can provide an Sb-rich environment. Sb_2Te_3 has a rhombohedral structure and there are five atomic layers in it: Te^1-Sb-Te^2-Sb-Te^1. In an Sb-rich thin film, the Sb′ **Te** antisite defects are easy to occur at the Te^1 site due to the lower formation energy of Sb′ Te1 (0.47 eV) compared to Sb′ Te2 (0.76 eV).[24] The Sb′ **Te** introduces extra hole carriers, and in comparison to other samples, the SO:ST = 1:1000 sample exhibits a higher concentration of free holes.[25] All of these effects interact and compete with each other, ultimately resulting in an increase in carrier concentration and conductivity for the SO:ST = 1:1000 sample.

The SbO_x/Sb_2Te_3 samples underwent detailed microstructural characterizations using transmission electron microscopy (TEM). Figure 2h presents a typical high-resolution TEM (HRTEM) image of the SL, clearly illustrating the remarkably uniform interface between the Sb_2Te_3 and SbO_x layers. Nonetheless, some atomic-scale distortions are still observable within this system. Various dash lines in Figure 2i indicate twin boundaries at different angles. Twin boundaries and semicoherent interfaces induce enhanced phonon scattering while causing only minimal sacrifice in electrical conductivity.[26] These defects significantly contribute to the scattering of mid-frequency phonons and contribute to the softening of the lattice, thereby effectively affecting the electrical and thermal conductivity of the material.[27]

To better understand the impact of SbO_x sub-layers on the Sb_2Te_3 thin film, the carrier concentration, and conductivity of Sb_2Te_3 thin film with varying SbO_x sub-cycle numbers were evaluated, as displayed in **Figure 3**a,b, respectively. The cycles of Sb_2Te_3 layers are 1000, 600, 300, and 150, combined with the 1, 3, 5, and 10 sub-cycles of SbO_x. It is observed that the carrier concentration and conductivity of all the samples decreased with increasing SbO_x sub-layers. For example, the n and σ for the sample SO:ST = 1:600 are 9.20×10^{18} cm^{-3} and 255.6 S cm^{-1}, respectively, at room temperature. When the sub-cycles of SbO_x increased to 10, the n and σ decreased to 6.51×10^{18} cm^{-3} and

© 2023 The Authors. Small published by Wiley-VCH GmbH

16136829, 2024, 10, Downloaded from https://onlinelibrary.wiley.com/doi/10.1002/smll.202306350, Wiley Online Library on [13/04/2024]. See the Terms and Conditions (https://onlinelibrary.wiley.com/terms-and-conditions) on Wiley Online Library for rules of use; OA articles are governed by the applicable Creative Commons License

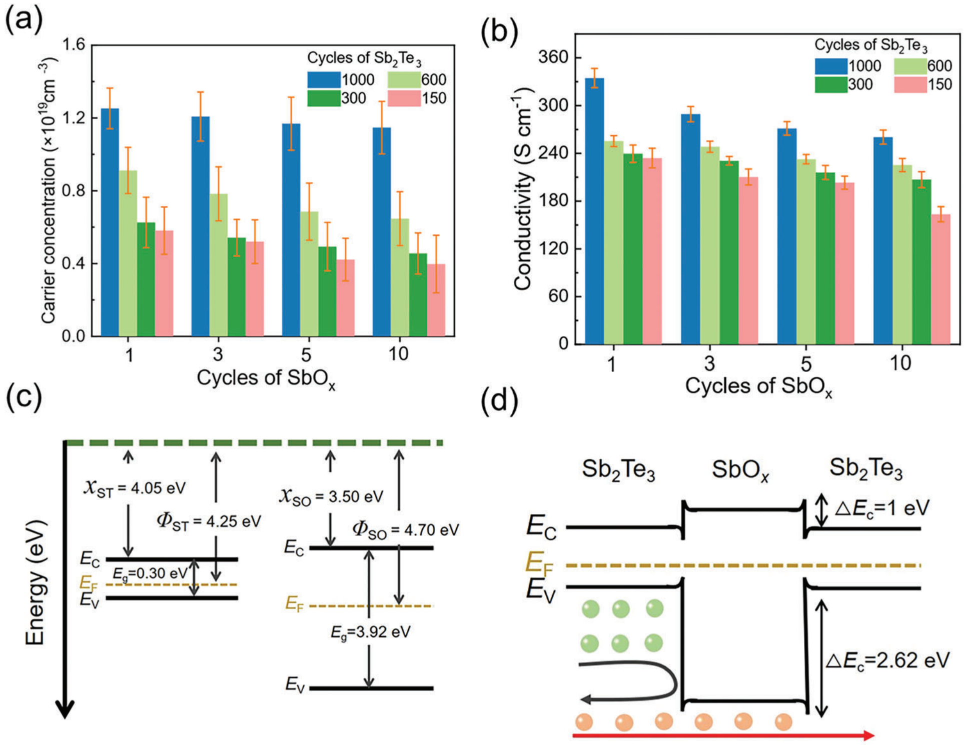

Figure 3. The carrier concentration (a) and conductivity (b) of SO/ST heterostructure with different SbO$_x$ sublayer cycles at room temperature. Energy band structure for c) Sb$_2$Te$_3$ and SbO$_x$ individual, and d) SbO$_x$/Sb$_2$Te$_3$ superlattice film.

225.8 S cm^{-1}, respectively. This can be attributed to energy filtering, where the SbO$_x$ interfacial layer effectively filters out holes from participating in carrier transport in the Sb$_2$Te$_3$ system.[28]

The energy band structure, including band gap (E_g), work function (Φ), electron affinity (χ), and Fermi level (E_F), for Sb$_2$Te$_3$, SbO$_x$, and SO/ST heterostructure are shown in Figure 3c,d.[19] Under equilibrium conditions, an energy barrier forms at the Sb$_2$Te$_3$ and SbO$_x$ interface due to the alignment of the Fermi level. In SO/ST SLs, low kinetic energy minority carriers can be blocked by two kinds of barriers: grain boundaries and band offset potential barriers,[28] the potential barrier being the primary contributor to modulating the charge carriers.[29] This energy barrier reduces low-energy carriers while having minimal impact on high-energy holes, resulting in a decrease in carrier concentration and conductivity. Therefore, as the sub-cycle number of SbO$_x$ increases, the n and σ of all the samples decrease. However, for the SO:ST = 5:150 sample, the n is 4.22×10^{18} cm^{-3}, while for the SO:ST = 10:150 sample, it is approximately 3.97×10^{18} cm^{-1}. This decrease was only 5.9%. Comparatively, the n of sample SO:ST = 3:150 exhibits a clear decrease of 18.8% compared to sample SO:ST = 5:150 (from 5.20×10^{18} to 4.22×10^{18} cm^{-3}). We assume that the SbO$_x$ could strengthen the energy barrier and further reduce the low energy carriers. Once the stable SbO$_x$ layer has been formed, the additional filtering effect on the carriers becomes negligible.

Figure 4a shows the Seebeck coefficient of Sb$_2$Te$_3$ thin films with various SbO$_x$ sub-layers at room temperature. The sample characterized by SO:ST = 10:150 exhibited the greatest S value at 157.8 μV K^{-1}, ≈1.25 times higher than that of Sb$_2$Te$_3$ films. This difference may be attributed to the lower carrier concentration found in the heterostructure of SO/ST when compared to Sb$_2$Te$_3$. For a multilayered thin film system, the Seebeck coefficient can be explained by the Cutler–Mott formula[30]

$$S = \frac{4\pi^3 k_B^2 T m^*}{3eh^2} \times \frac{1}{n \times L_2} \tag{3}$$

where k_B is the Boltzmann constant, h is the Planck constant, m^* is the effective mass, n is the carrier concentration, and L_2 is the thickness of the interlayer in the superlattice film (here SbO$_x$ layer), respectively. It can be observed that two primary factors contribute to determining the Seebeck coefficient: carrier concentration and sub-layer thickness. Specifically, a thinner SbO$_x$ interlayer and lower carrier concentration can lead to an improved Seebeck coefficient. Hence, the S values of the SO/ST SLs are the outcome of the interplay between the influence of carrier concentration and the thickness of SbO$_x$.[31] The power factor is depicted in Figure 4b. At room temperature, the maximum PF of 530.7 μW m^{-1} K^{-2} was achieved when SO:ST = 10:1000. In contrast, the sample with SO:ST = 10:150 has a low PF of 407.2 μW m^{-1} K^{-2} owing to its low electrical conductivity.

The Raman spectra and corresponding vibration are shown in Figure 4c and Figure S4, Supporting Information, respectively. The peak centered at ≈70 and 168 cm^{-1} can be assigned to the $A_{1g}(1)$ and $A_{1g}(2)$ phonon modes, respectively. $A_{1g}(1)$ is primarily associated with symmetrical out-of-plane vibrations of Sb—Te atoms occurring in opposite directions, while $A_{1g}(2)$ is associated with relative vibration between Te and Sb atoms in the same

© 2023 The Authors. Small published by Wiley-VCH GmbH

16136829, 2024, 10, Downloaded from https://onlinelibrary.wiley.com/doi/10.1002/smll.202306350, Wiley Online Library on [13/04/2024]. See the Terms and Conditions (https://onlinelibrary.wiley.com/terms-and-conditions) on Wiley Online Library for rules of use; OA articles are governed by the applicable Creative Commons License

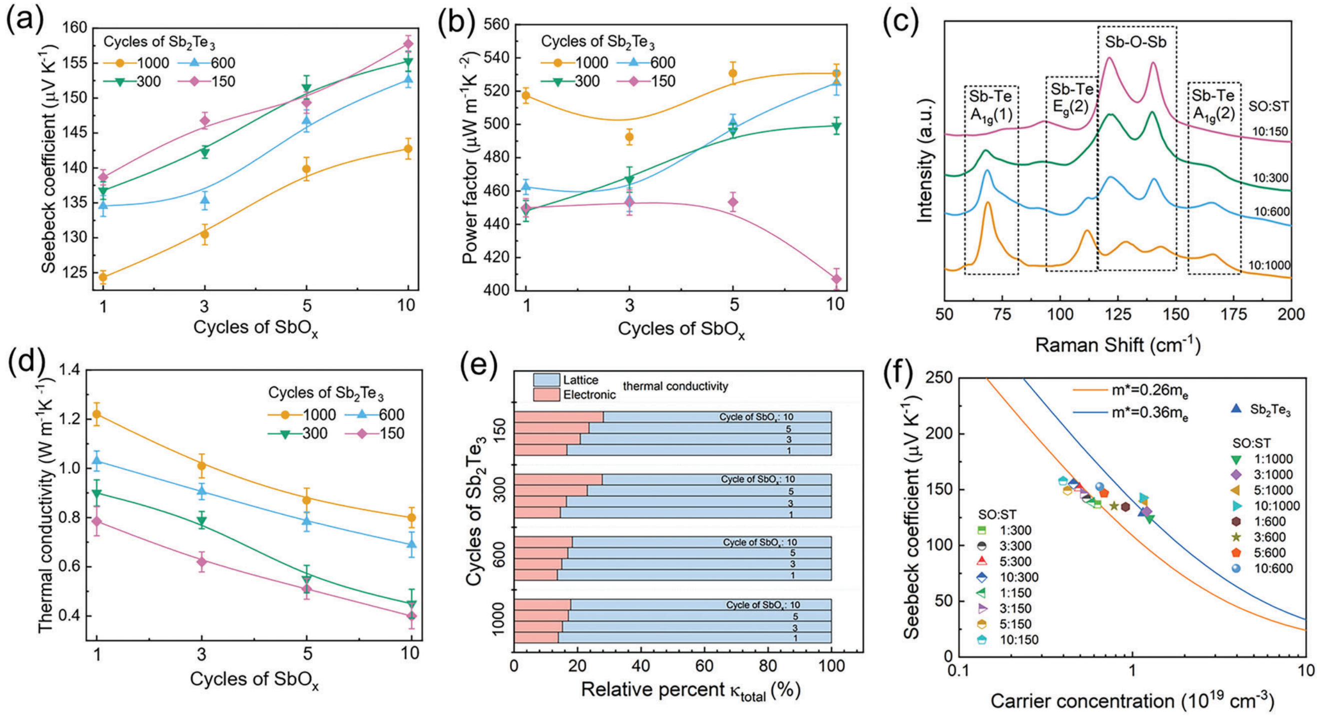

Figure 4. Thermoelectric performance of SO/ST heterostructure with SbO_x sublayer cycles at room temperature. a) Seebeck coefficient, b) power factor, c) Raman spectra, d) thermal conductivity, and e) relative contribution of the electronic (κ_{E}) and lattice (κ_{L}) thermal conductivities to the total thermal conductivity (κ_{Total}). f) Seebeck coefficient as a function of Hall carrier concentration at room temperature (m_{e} is the mass of a free electron).

direction. The peak at 112.3 cm^{-1} is linked to the in-plane $E_g(2)$ mode.[32] The peaks ranging from ≈120 to 150 cm^{-1} can be assigned to vibrations of Sb—O—Sb atoms.[33] The vibration modes for Sb—O become stronger with increasing sub-cycle number of SbO_x, while Sb—Te peaks almost disappear when SO:ST = 10:150. The $E_g(2)$ mode reflects the lattice strain within the heterostructure system, which is closely correlated with the lattice thermal conductivity.[34] The broadening of the $E_g(2)$ mode indicates an increase in the lattice strain of $\mathrm{Sb_2Te_3}$ layers, thereby leading to a reduction of the lattice thermal conductivity.[35] The thermal conductivity of SO/ST heterostructure was evaluated at room temperature using the 3-ω technique. Figure 4d shows that the total thermal conductivity (κ_{Total}) of the samples substantially decreases with an increase in SbO_x sub-cycles. This reduction of κ_{Total} remains constant as the number of ALD cycles for SbO_x increases. The κ_{Total} values for $\mathrm{Sb_2Te_3}$ with ten cycled SbO_x sub-layers were measured to be ≈0.80, ≈0.69, ≈0.45, and ≈0.40 W m^{-1} K^{-1} for respective $\mathrm{Sb_2Te_3}$ thicknesses of 1000, 600, 300, and 150 cycles. The minimum thermal conductivity (SO:ST = 10:150) is ≈3.05 times lower than the maximum thermal conductivity of the SO:ST = 1:1000 sample. To further understand the thermal behavior of SO/ST structures, the electronic (κ_{E}) and lattice (κ_{L}) thermal conductivities were carried out by the Wiedemann–Franz law[36]

$$\kappa_{\mathrm{E}} = L\sigma T \tag{4}$$

$$L = 1.5 + \exp\left[\frac{|S|}{116}\right] \tag{5}$$

$$\kappa_{\mathrm{Total}} = \kappa_L + \kappa_E \tag{6}$$

where L is Lorenz number, T is the temperature, and S is the Seebeck coefficient, respectively. The κ_{E} and κ_{L} are shown in Figures S5 and S6, Supporting Information, respectively. The relative contribution of the electronic and lattice thermal conductivities to the total thermal conductivity is shown in Figure 4e. In the SO/ST heterostructure, lattice thermal conductivity primarily contributes to the total thermal conductivity. The interface between SbO_x and $\mathrm{Sb_2Te_3}$ enhances the scattering phonons with mid- to long-wavelengths, which is considerably more efficient than that of normal grain boundaries, thus reducing κ_{L} in the SO/ST heterostructure system.[16] Additionally, when the dimensions of materials are reduced to the nanometer length scales, the band structure exhibits a more flattened profile due to the quantum confinement effect. This leads to the formation of sharp peaks in the density of states, resulting in an enhanced Seebeck coefficient and reduced thermal conductivity.[37] A maximum ZT value of 0.33 was achieved for the sample SO:ST = 10:300 (Figure S7, Supporting Information), primarily attributable to the low thermal conductivity.

Single parabolic band (SPB) is the most widely used approach to evaluate the electrical transport property of thermoelectric materials.[38] The relationship between the Seebeck coefficient and carrier concentration at room temperature was established by the Pisarenko plot, as depicted in Figure 4f. The effective mass of $\mathrm{Sb_2Te_3/SbO}_x$ heterostructure, m^*, decreases from 0.36 m_{e} for the low doping level of SbO_x to 0.26 m_{e} for the high doping level. The SbO_x sub-layers can suppress the multivalence band convergence and valence band flattening, which further reduces m^*.[39]

© 2023 The Authors. Small published by Wiley-VCH GmbH

16136829, 2024, 10, Downloaded from https://onlinelibrary.wiley.com/doi/10.1002/smll.202306350, Wiley Online Library on [13/04/2024]. See the Terms and Conditions (https://onlinelibrary.wiley.com/terms-and-conditions) on Wiley Online Library for rules of use; OA articles are governed by the applicable Creative Commons License

16136829, 2024, 10, Downloaded from https://onlinelibrary.wiley.com/doi/10.1002/smll.202306350, Wiley Online Library on [13/04/2024]. See the Terms and Conditions (https://onlinelibrary.wiley.com/terms-and-conditions) on Wiley Online Library for rules of use; OA articles are governed by the applicable Creative Commons License

3. Conclusion

In conclusion, the SbO_x/Sb_2Te_3 heterostructures were successfully synthesized by thermal ALD at a low temperature of 80 °C. The electrical and thermal properties, including carrier concentration, electrical conductivity, Seebeck coefficient, and thermal conductivity, were evaluated. The SbO_x sub-cycle can enhance the texture and promote the preferred orientation of Sb_2Te_3 layers. By optimizing the sub-cycle number of the SbO_x layer, a high power factor of 520.8 $\mu W\ m^{-1}\ K^{-2}$ was obtained when SO:ST = 1:1000, which had a higher electrical conductivity of 339.8 $S\ cm^{-1}$ compared to Sb_2Te_3 (291.9 $S\ cm^{-1}$) films. SbO_x/Sb_2Te_3 interface can scatter more mid- to long-wavelength phonons, which is much more efficient in reducing thermal conductivity than normal grain boundaries. In addition, the quantum confinement effect and lattice strain introduced by the SbO_x sub-layer can further reduce the thermal conductivity and improve the Seebeck coefficient. The minimum total thermal conductivity of ≈0.4 $W\ m^{-1}\ K^{-1}$ was obtained for the sample SO:ST = 10:150. This study not only provides strong evidence of the potential for enhancing TE performance through the introduction of a superlattice structure via ALD but also suggests a new approach to achieving high performance in 2D topological insulator families.

4. Experimental Section

Fabrication of Sb_2Te_3 and SbO_x Thin Films: The Sb_2Te_3 and SbO_x thin film were grown using a thermal ALD reactor (Veeco Savannah S200) at 80 °C. For the synthesis of Sb_2Te_3 films, $SbCl_3$ and $(Et_3Si)_2Te$ precursors were employed, while $Sb(OEt)_3$ and $SbCl_3$ were used for the synthesis of SbO_x films. The $SbCl_3$ precursor was maintained at a temperature of 60 °C, while the $(Et_3Si)_2Te$ precursor was kept at 77 °C. High-purity N_2 was used as the carrier gas, and the chamber was kept at a flow rate of 10 sccm during the reaction process. The optimized pulse and purge times for one ALD deposition cycle for Sb_2Te_3 and SbO_x (Precursor 1/N_2/Precursor 2/N_2) were 0.5/10/0.5/10 s. The growth rate for Sb_2Te_3 and SbO_x are 0.2 and 0.6 Å/cycle, respectively. The details for heterostructure growth are illustrated in Figure S1 and Table S1, Supporting Information.

Characterization of Morphology, Electrical, and Thermal Properties: The thin film thickness was measured using X-ray reflectometry (X'Pert MRD PRO). The morphology and microstructures of the thin films were characterized by field emission scanning electron microscopy (FE-SEM, Sigma300-ZEISS FE-SEM) and TEM (Titan 80–300 and Talos F200X, FEI). The electrical conductivities and Hall effect were performed by Linseis TFA.[40] All photolithography steps were carried out using a laser writer (µPG 101, Heidelberg Instruments GmbH, Germany) with a 375 nm irradiation wavelength. In the initial step, a photoresist (AZ10XT, MicroChemicals GmbH, Germany) and developer (AZ400K, MicroChemicals GmbH, Germany) were employed to create pattern alignment markers and deposit the thin film on the Linseis TFA-chip. The curing temperature was set at 110 °C for 2 min. Subsequently, the photoresist was removed using *n*-methyl pyrrolidone (NMP). The transport properties were assessed over a temperature range of 293 to 473 K.

Supporting Information

Supporting Information is available from the Wiley Online Library or from the author.

Acknowledgements

This work was supported by the Program of Collaborative Research Centers in Germany (Grant No.: SFB 1415).

Open access funding enabled and organized by Projekt DEAL.

Conflict of Interest

The authors declare no conflict of interest.

Data Availability Statement

The data that support the findings of this study are available from the corresponding author upon reasonable request.

Keywords

atomic layer deposition, interface engineering, nanothermoelectricity, SbO_x/Sb_2Te_3, transport property

Received: July 26, 2023
Revised: September 22, 2023
Published online: October 25, 2023

---

[1] a) L. Deng, Y. Liu, Y. Zhang, S. Wang, P. Gao, *Adv. Funct. Mater.* **2023**, *33*, 2210770; b) Z. H. Zheng, X. L. Shi, D. W. Ao, W. D. Liu, M. Li, L. Z. Kou, Y. X. Chen, F. Li, M. Wei, G. X. Liang, P. Fan, G. Q. Lu, Z. G. Chen, *Nat. Sustainability* **2022**, *6*, 180.

[2] a) T.-R. Wei, P. Qiu, K. Zhao, X. Shi, L. Chen, *Adv. Mater.* **2023**, *35*, 2110236; b) D. W. Ao, W. D. Liu, Z. H. Zheng, X. L. Shi, M. Wei, Y. M. Zhong, M. Li, G. X. Liang, P. Fan, Z. G. Chen, *Adv. Energy Mater.* **2022**, *12*, 2202731; c) D.-W. Ao, W.-D. Liu, Y.-X. Chen, M. Wei, B. Jabar, F. Li, X.-L. Shi, Z.-H. Zheng, G.-X. Liang, X.-H. Zhang, P. Fan, Z.-G. Chen, *Adv. Sci. (Weinheim, Ger.)* **2022**, *9*, e2103547.

[3] Z.-H. Zheng, D.-L. Zhang, B. Jabar, T.-B. Chen, M. Nisar, Y.-F. Chen, F. Li, S. Chen, G.-X. Liang, X.-H. Zhang, P. Fan, Y.-X. Chen, *Mater. Today Phys.* **2022**, *24*, 100659.

[4] a) L. Hu, T. Zhu, X. Liu, X. Zhao, *Adv. Funct. Mater.* **2014**, *24*, 5211; b) J. H. Grebenkemper, S. Klemenz, B. Albert, S. K. Bux, S. M. Kauzlarich, *J. Solid State Chem.* **2016**, *242*, 55; c) J. He, T. M. Tritt, *Science* **2017**, *357*, eaak9997.

[5] L. D. Hicks, M. S. Dresselhaus, *Phys. Rev. B* **1993**, *47*, 12727.

[6] L. D. Hicks, T. C. Harman, X. Sun, M. S. Dresselhaus, *Phys. Rev. B* **1996**, *53*, R10493.

[7] a) A. I. Hochbaum, R. Chen, R. D. Delgado, W. Liang, E. C. Garnett, M. Najarian, A. Majumdar, P. Yang, *Nature* **2008**, *451*, 163; b) J. P. Heremans, V. Jovovic, E. S. Toberer, A. Saramat, K. Kurosaki, A. Charoenphakdee, S. Yamanaka, G. J. Snyder, *Science* **2008**, *321*, 554.

[8] D. Van Tuan, M. Yang, H. Dery, *Phys. Rev. B* **2018**, *98*, 125308.

[9] G. Chen, **1999**.

[10] G. Chen, *Phys. Rev. B* **1998**, *57*, 14958.

[11] J. Yang, J. Li, A. Bahrami, N. Nasiri, S. Lehmann, M. O. Cichocka, S. Mukherjee, K. Nielsch, *ACS Appl. Mater. Interfaces* **2022**, *14*, 54034.

[12] M. Winkler, *Doctoral dissertation*, Universität Tübingen, **2015**.

[13] N.-W. Park, W.-Y. Lee, Y.-S. Yoon, G.-S. Kim, Y.-G. Yoon, S.-K. Lee, *ACS Appl. Mater. Interfaces* **2019**, *11*, 38247.

[14] G. Yang, J. Pan, X. Fu, Z. Hu, Y. Wang, Z. Wu, E. Mu, X.-J. Yan, M.-H. Lu, *Nano Convergence* **2018**, *5*, 22.

[15] a) J. Yang, A. Bahrami, X. W. Ding, S. Lehmann, N. Kruse, S. Y. He, B. W. Wang, M. Hantusch, K. Nielsch, *Adv. Mater. Interfaces* **2022**, *9*, 2101953; b) J. Yang, Y. Zhang, Q. Wu, C. Dussarrat, J. Qi, W. Zhu, X. Ding, J. Zhang, *IEEE Trans. Electron Devices* **2019**, *66*, 3382; c) Y. Kim, W. J. Woo, D. Kim, S. Lee, S.-M. Chung, J. Park, H. Kim, *Adv. Mater.* **2021**, *33*, 2005907.

[16] N.-W. Park, W.-Y. Lee, Y.-S. Yoon, J.-Y. Ahn, J.-H. Lee, G.-S. Kim, T. G. Kim, C.-J. Choi, J.-S. Park, E. Saitoh, S.-K. Lee, *ACS Appl. Mater. Interfaces* **2018**, *10*, 44472.

© 2023 The Authors. Small published by Wiley-VCH GmbH

[17] W.-Y. Lee, N.-W. Park, S.-Y. Kang, G.-S. Kim, J.-H. Koh, E. Saitoh, S.-K. Lee, *J. Phys. Chem. C* **2019**, *123*, 14187.
[18] K. Liu, B. Jin, W. Han, X. Chen, P. Gong, L. Huang, Y. Zhao, L. Li, S. Yang, X. Hu, J. Duan, L. Liu, F. Wang, F. Zhuge, T. Zhai, *Nat. Electron.* **2021**, *4*, 906.
[19] J. Yang, A. Bahrami, X. W. Ding, P. P. Zhao, S. Y. He, S. Lehmann, M. Laitinen, J. Julin, M. Kivekas, T. Sajavaara, K. Nielsch, *Adv. Electron. Mater.* **2022**, *8*, 2101334.
[20] M. Naumochkin, G. H. Park, K. Nielsch, H. Reith, *Phys. Status Solidi RRL* **2022**, *16*, 2100533.
[21] a) K. Pal, S. Anand, U. V. Waghmare, *J. Mater. Chem. C* **2015**, *3*, 12130; b) N. V. C. Shekar, D. A. Polvani, J. F. Meng, J. V. Badding, *Phys. B* **2005**, *358*, 14.
[22] a) J. Zhang, T. Hu, J. Yan, F. Ke, J. Wang, X. Cui, X. Li, Y. Ma, J. Yang, C. Gao, *Mater. Lett.* **2017**, *209*, 78; b) O. Gomis, R. Vilaplana, F. J. Manjón, P. Rodríguez-Hernández, E. Pérez-González, A. Muñoz, V. Kucek, C. Drasar, *Phys. Rev. B* **2011**, *84*, 174305.
[23] J. Yang, A. Bahrami, X. Ding, S. Lehmann, K. Nielsch, *Appl. Phys. Lett.* **2022**, *121*, 163504.
[24] T. Thonhauser, G. S. Jeon, G. D. Mahan, J. O. Sofo, *Phys. Rev. B* **2003**, *68*, 205207.
[25] Z.-W. Sun, K.-W. Cheng, S.-W. Lin, V. K. Ranganayakulu, Y.-Y. Chen, S.-J. Chiu, T.-W. Lee, A. T. Wu, *ACS Appl. Energy Mater.* **2022**, *5*, 7026.
[26] S. Li, W. Zhao, Y. Cheng, L. Chen, M. Xu, K. Guo, F. Pan, *ACS Appl. Mater. Interfaces* **2022**, *15*, 1167.
[27] S. Li, Z. Huang, R. Wang, W. Zhao, J. Luo, Y. Xiao, F. Pan, *ACS Appl. Mater. Interfaces* **2021**, *13*, 51018.
[28] W. Y. Lee, N. W. Park, S. Y. Kang, M. S. Kang, T. T. T. Bui, J. Seok, G. S. Kim, E. Saitoh, S. K. Lee, *J. Alloys Compd.* **2020**, *815*, 152482.
[29] a) C. Zhang, H. Ng, Z. Li, K. A. Khor, Q. Xiong, *ACS Appl. Mater. Interfaces* **2017**, *9*, 12501; b) H. Yang, J.-H. Bahk, T. Day, A. M. S. Mohammed, G. J. Snyder, A. Shakouri, Y. Wu, *Nano Lett.* **2015**, *15*, 1349.
[30] S. Shimizu, M. S. Bahramy, T. Iizuka, S. Ono, K. Miwa, Y. Tokura, Y. Iwasa, *Proc. Natl. Acad. Sci. U. S. A.* **2016**, *113*, 6438.
[31] D. A. Broido, T. L. Reinecke, *Phys. Rev. B* **2001**, *64*, 045324.
[32] H. Zhang, X. Zhang, C. Liu, S. T. Lee, J. Jie, *ACS Nano* **2016**, *10*, 5113.
[33] Z. Sui, S. Hu, H. Chen, C. Gao, H. Su, A. Rahman, R. Dai, Z. Wang, X. Zheng, Z. Zhang, *J. Mater. Chem. C* **2017**, *5*, 5451.
[34] Z. H. Wu, X. Chen, E. Z. Mu, Y. Liu, Z. X. Che, C. C. Dun, F. Y. Sun, X. W. Wang, Y. L. Zhang, Z. Y. Hu, *Adv. Electron. Mater.* **2020**, *6*, 1900735.
[35] Y. Wu, Z. Chen, P. Nan, F. Xiong, S. Lin, X. Zhang, Y. Chen, L. Chen, B. Ge, Y. Pei, *Joule* **2019**, *3*, 1276.
[36] M. Jonson, G. D. Mahan, *Phys. Rev. B* **1980**, *21*, 4223.
[37] Z. Gao, X. Ning, J. Wang, J. Wang, S. Wang, *Small* **2022**, *18*, e2104916.
[38] a) H. Naithani, T. Dasgupta, *ACS Appl. Energy Mater.* **2019**, *3*, 2200; b) J. B. Zhu, X. M. Zhang, M. C. Guo, J. Y. Li, J. S. Hu, S. T. Cai, W. Cai, Y. S. Zhang, J. H. Sui, *npj Comput. Mater.* **2021**, *7*, 116.
[39] Y. Huang, S. Zhi, S. Zhang, W. Yao, W. Ao, C. Zhang, F. Liu, J. Li, L. Hu, *Materials* **2022**, *15*, 6798.
[40] V. Linseis, F. Völklein, H. Reith, K. Nielsch, P. Woias, *Rev. Sci. Instrum.* **2018**, *89*, 015110.

© 2023 The Authors. Small published by Wiley-VCH GmbH

16136829, 2024, 10, Downloaded from https://onlinelibrary.wiley.com/doi/10.1002/smll.202306350, Wiley Online Library on [13/04/2024]. See the Terms and Conditions (https://onlinelibrary.wiley.com/terms-and-conditions) on Wiley Online Library for rules of use; OA articles are governed by the applicable Creative Commons License